Supporting Information Appendix to

Nature does not rely on long-lived electronic quantum coherence for photosynthetic energy transfer

Hong-Guang Duan, Valentyn I. Prokhorenko, Richard J. Cogdell, Khuram Ashraf, Amy L. Stevens, Michael Thorwart*, R. J. Dwayne Miller*

*Corresponding authors.

E-mail: michael.thorwart@physik.uni-hamburg.de, dwayne.miller@mpsd.mpg.de

Preparation of the FMO protein

The Fenna-Matthews-Olson (FMO) protein complex was prepared from cells of the thermophilic green sulfur bacterium *Chlorobium tepidum*. A strain of *C. tepidum* that had been engineered to produce a His-tagged version of its reaction center was used in order to simplify the purification strategy. This strain was a gift of Prof. Oh-Oka (*1*). The cells were grown anaerobically in the light in modified Pfennig's media (*2*). New cultures were allowed to go fully anaerobic in the dark overnight, then they were grown at a light intensity of about 30 micromoles photons $m^{-2}s^{-1}$ at 43° C for 2 to 3 days. When fully grown, the cells were harvested by centrifugation at 12,000 x g for 20 min. The reaction centres (which bind FMO) were isolated from broken cells (*3*). At the stage of the nickel affinity column chromatography a high salt wash at 500 mM NaCl elutes the FMO complexes. This dilute solution of FMO was then purified by a combination of ion exchange chromatography on a Whatrman DE52 cellulose resin and size exclusion chromatography on a Sepharose S-200 column.

Sample condition at room temperature

Before doing the measurement, we have checked the thermal degradation of the sample for different temperatures. The sample was kept under -80° C in the freezer. Before measuring the circular dichroism (CD) spectrum, we have warmed up the sample by putting it on the table for about half an hour. Then, we have recorded the CD spectrum in the UV region at the temperature of 23° C, at which we have recorded the 2D spectra. The result of the CD spectrum is shown in Fig. S1 (a). We extract the structure information of the FMO protein by measuring

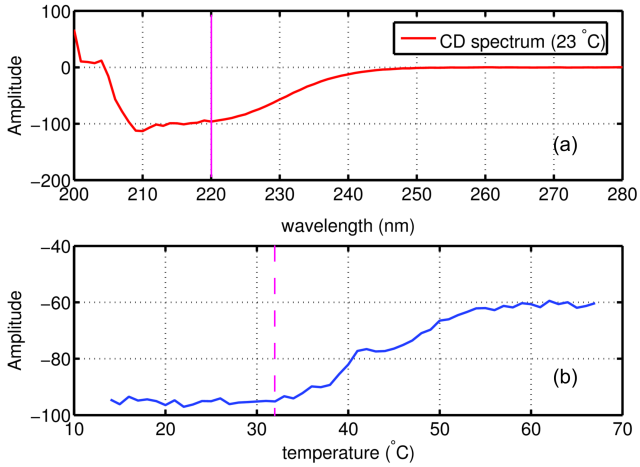

Figure S1: (a) Circular dichroism (CD) spectrum of the FMO complex in the UV regime at room temperature (23° C). The magenta solid line marks the wave length of 220 nm at which we detect the sample condition. (b) CD spectral signal at 220 nm for varying temperature. The magenta dashed line marks the temperature (32° C) above which thermal degradation of the FMO protein sets in.

the signal changes at the wave length of 220 nm (*4, 5*). Usually, the signal at this frequency is considered as originating from the protein. It shows a relatively strong magnitude with a weak noisy background. It is marked by the magenta line in the Fig. S1 (a). Then, we have recorded the CD spectra at different temperatures starting from 14 to 67° C. The result of the CD spectral signal at 220 nm for different temperatures is shown in Fig. S1 (b). We observe that the CD signal is stable and shows $\sim$ 95 counts below 32° C. Above 32° C, the magnitude of the CD signal at 220 nm rapidly decays to 60 counts. This indicates that the structure of the protein experiences thermal damage. We have repeated the detection five times at each temperature and show the corresponding average in the figure.

Laser excitation spectrum and field strength

The excitation spectrum of the laser used was a broadband spectrum with a FWHM of 100 nm, centered at the wavelength of 770 nm and overlapped the Q_y absorption band of the FMO antenna complex (see Fig. S2 (a)). The excitation energy was kept below 12 nJ per beam to stay in the weak-field regime of linear excitation. The magnitude of the detected homodyne photon-echo signal was proportional to the third power of the incoming pulse energy, see Fig. S2 (b).

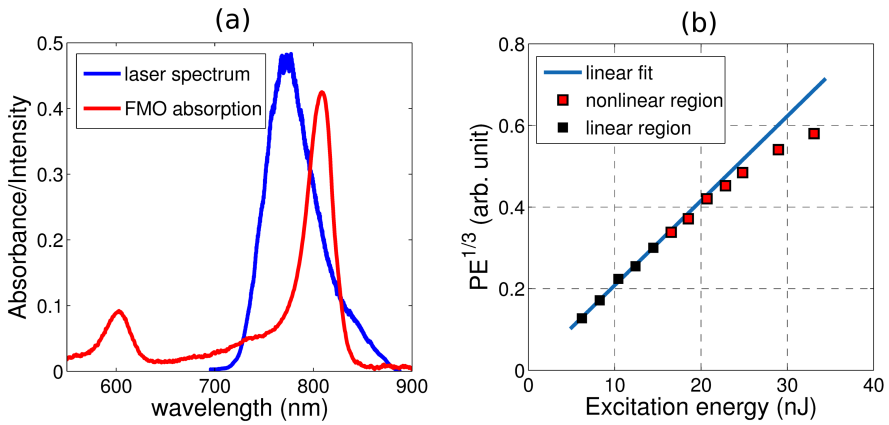

Figure S2: (a) Laser excitation spectrum (blue line) and absorption spectrum (red line) of the FMO complex at room temperature. (b) Dependence of the homodyne photon echo signal on the excitation energy measured at zero waiting time. To illustrate the deviation from the linear region, we plot the cubic root of the magnitude of the photon echo signal on the ordinate.

Spectral density

For simplicity, we choose an Ohmic spectral density to characterize the environmental fluctuations. In addition, to account for the weak vibrational progression detected in the absorption spectrum of the FMO complex (see Fig. 1C in the main paper), we have to add one additional vibrational mode in the spectral density. We find an optimal fit if we assume this component to be of the form of an overdamped harmonic mode to phenomenologically cover the experimentally observed vibrational sidebands in the linear spectrum (*6*). Therefore, the total spectral density used throughout the work is

$$J(\omega) = \gamma\omega e^{-\omega/\omega_c} + \frac{2}{\pi} S\Omega^3 \frac{\omega\Gamma}{(\Omega^2-\omega^2)^2+\omega^2\Gamma^2}\,. \tag{S1}$$

Here, γ is the Ohmic damping constant and ω_c is a high-frequency cut-off parameter. Moreover, S is the Huang-Rhys factor, Ω is the vibrational frequency of the overdamped mode and Γ is the lifetime broadening. From fitting the linear absorption spectrum, we find $\gamma = 0.7$, $\omega_c = 350$ cm^{-1}, $S = 0.12$, $\Omega = 900$ cm^{-1} and $\Gamma = 700$ cm^{-1}. The reorganization energy can be calculated as $\lambda = \frac{2}{\pi}\gamma\omega_c + \frac{1}{\pi}S\Omega = 190$ cm^{-1}. The spectral density is shown in Fig. S3.

Time non-local quantum master equation

For the numerical simulations, we have applied the established method of the time non-local quantum master equation (*7, 8*). Time evolution of the total density matrix ρ which includes system and bath is governed by the Liouville-von Neumann equation with the Liouville super-

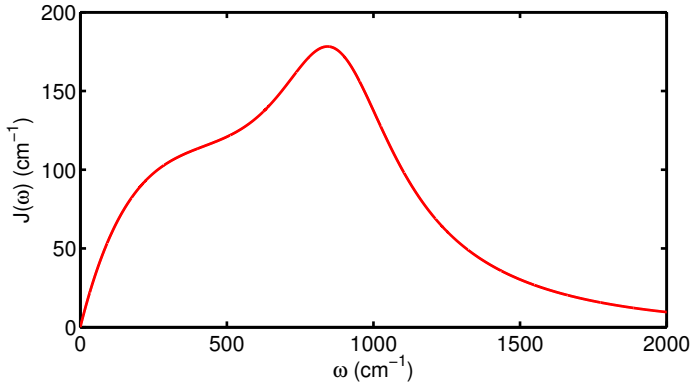

Figure S3: Spectral density used in this work for modeling the dissipative exciton dynamics. The overdamped mode yields the accurate vibrational progression in the absorption spectrum of the FMO complex shown in Fig. 1C in the main paper.

operator $\mathcal{L}$ ($\hbar = 1$), according to

$$\dot{\rho}_{\rm tot} = -i[H_{\rm tot}, \rho_{\rm tot}] = \mathcal{L}\rho_{\rm tot}\,. \tag{S2}$$

The total Hamiltonian $H_{\rm tot} = H_{\rm s} + H_{\rm b} + \lambda H_{\rm sb} + \lambda^2 H_{\rm ren}$ includes the system, the bath, and interaction and renormalization terms. For the sake of concreteness, let us assume here a system with a single degree of freedom x. The bath consists of an ensemble of harmonic oscillators with the Hamiltonian $H_{\rm b} = \sum_{j=1}^{N}\left[p_j^2/(2m_j) + m_j\omega_j^2 x_j^2/2\right]$. The coupling between them is assumed in form $H_{\rm sb} = f(x)\sum_{j=1}^{N} c_j x_j$ with some real function $f(\cdot)$.

The projection scheme of Nakajima and Zwanzig (*9*) allows us to separate the dynamics of system and bath. The thermal state of the bath is represented by the canonical density operator $\rho_{\rm b}^{\rm eq} = \exp(-\beta H_{\rm b})/Z_{\rm b}$ with a given temperature $T = (k_B\beta)^{-1}$ and $Z_{\rm b}$ being the partition function of the bath. Applying a projector $P = \rho_{\rm b}^{\rm eq}{\rm tr}_{\rm b}$ with ${\rm tr}_{\rm b}\rho_{\rm b}^{\rm eq} = 1$ and $Q = (1-P)$ yields an exact formal quantum master equation for the time evolution of the reduced system density operator $\rho_{\rm s}$ (*7*) in the form

$$\begin{aligned}
\dot{\rho}_{\rm s}(t) &= \mathcal{L}_{\rm s}^{\rm eff}\rho_{\rm s}(t) + \int_0^t dt' K(t,t')\rho_{\rm s}(t') + \Gamma(t),\\
\mathcal{L}_{\rm s}^{\rm eff} &= \mathcal{L}_{\rm s} + \lambda\,{\rm tr}_{\rm b}\mathcal{L}_{\rm sb}\rho_{\rm b}^{\rm eq} + \lambda^2\mathcal{L}_{\rm ren},\\
K(t,t') &= \lambda\,{\rm tr}_{\rm b}\mathcal{L}_{\rm sb}\left(\mathcal{T}e^{\int_{t'}^{t} Q\mathcal{L}dt''}\right)Q(\mathcal{L}_{\rm b} + \lambda\mathcal{L}_{\rm sb})\rho_{\rm b}^{\rm eq},\\
\Gamma(t) &= \lambda\,{\rm tr}_{\rm b}\mathcal{L}_{\rm sb}\left(\mathcal{T}e^{\int_{0}^{t} Q\mathcal{L}dt''}\right)Q\rho_{\rm tot}(0).
\end{aligned} \tag{S3}$$

Here, $\rho_{\rm tot}(0)$ is the total density operator of system and bath at initial time. The Liouville superoperators $\mathcal{L}_{\rm s}$, $\mathcal{L}_{\rm sb}$ and $\mathcal{L}_{\rm ren}$ are associated with corresponding Hamiltonian operators. Moreover,

$\mathcal{L}_{\rm s}^{\rm eff} = -i[H_{\rm s}+H_{\rm ren},\cdot]$ and $\mathcal{T}$ is the time-ordering operator (*10*). Next, we expand the correlated thermal equilibrium state to the first order in the overall coupling strength λ and obtain

$$\rho^{\rm eq} \approx \frac{1}{Z_{\rm s}}\frac{1}{Z_{\rm b}}e^{-\beta(H_{\rm s}+H_{\rm b})} - \lambda\frac{1}{Z_{\rm s}}\frac{1}{Z_{\rm b}}\int_0^\beta d\beta' e^{-(\beta-\beta')(H_{\rm s}+H_{\rm b})}H_{\rm sb}^{(1)}e^{-\beta'(H_{\rm s}+H_{\rm b})}, \tag{S4}$$

with the respective partition functions $Z_{\rm tot} = {\rm tr}\exp(-\beta H_{\rm tot})$, $Z_{\rm b} = {\rm tr}_{\rm b}\exp(-\beta H_{\rm b})$ and $Z_{\rm s} = {\rm tr}_{\rm s}\exp(-\beta H_{\rm s})$. Next, we take the trace over the system degrees of freedom on both sides of Eq. (S4) and get

$$\rho_{\rm b}^{\rm eq} = \frac{1}{Z_{\rm b}}e^{-\beta H_{\rm b}} + \frac{\lambda\chi}{Z_{\rm b}}\int_0^\beta d\beta' e^{-(\beta-\beta')H_{\rm b}}\left(\sum_{i=1}^N c_i x_i\right)e^{-\beta' H_{\rm b}}. \tag{S5}$$

Here, $\chi = (1/Z_{\rm s}){\rm tr}_{\rm s}\left[f(x)e^{-\beta H_{\rm s}}\right]$. The well-known bath correlation function

$$c(t) = \int_{-\infty}^{\infty}\frac{d\omega}{2\pi}J(\omega)\cos(\omega t)\coth\left(\frac{\beta\omega}{2}\right) - i\int_{-\infty}^{\infty}\frac{d\omega}{2\pi}J(\omega)\sin(\omega t) \equiv a(t) - ib(t) \tag{S6}$$

is given in terms of the standard bath spectral density $J(\omega)$ and has the real part $a(t)$ and imaginary part $b(t)$. After inserting Eqs. (S4) and (S5) into Eq. (S3), we can express the last three terms of Eq. (S3) by $a(t)$ and $b(t)$ and obtain

$$\begin{aligned}
\mathcal{L}_{\rm s}^{\rm eff} &= \mathcal{L}_{\rm s} + \lambda^2\mu\mathcal{L}_{\rm ren,s} + \lambda^2\chi\mu\mathcal{L}^-, \\
K(t,t') &= \lambda^2\mathcal{L}^-\left(a(t-t')\mathcal{T}e^{\int_{t'}^t\mathcal{L}_{\rm s}dt''}\mathcal{L}^- + b(t-t')\mathcal{T}e^{\int_{t'}^t\mathcal{L}_{\rm s}dt''}\mathcal{L}^+\right), \\
\Gamma(t) &= \lambda^2\mathcal{L}^-\int_{-\infty}^0 dt'\left[a(t-t')\mathcal{T}e^{\int_{t'}^t\mathcal{L}_{\rm s}dt''}\mathcal{L}^-\rho_{\rm s}^{\rm eq} + b(t-t')\mathcal{T}e^{\int_{t'}^t\mathcal{L}_{\rm s}dt''}\mathcal{L}^+\rho_{\rm s}^{\rm eq}\right],
\end{aligned} \tag{S7}$$

with $\mathcal{L}^- = -i[H_{\rm sb},\cdot]$ and $\mathcal{L}^+ = [H_{\rm sb},\cdot]_+ - 2\chi$. In terms of the spectral density, the potential renormalization is given by $\mu = \int_{-\infty}^{\infty}\frac{d\omega}{2\pi}J(\omega)/\omega$.

In order to obtain an analytic form of the bath correlation function, any given spectral density (in our particular case, we use the standard Ohmic form) can be approximated by a sum of Lorentzian-like spectral terms (*11, 12*) in the form

$$J(\omega) = \frac{\pi}{2}\sum_{k=1}^n\frac{p_k\omega}{[(\omega+\Omega_k)^2+\Gamma_k^2][(\omega-\Omega_k)^2+\Gamma_k^2]}, \tag{S8}$$

where the spectral amplitude p_k, the frequency Ω_k and the width Γ_k follows from the expansion of the original function in terms of Lorentzian functions. Inserting the expanded form of $J(\omega)$

in Eq. (S6) results in

$$
\begin{aligned}
a(t) &= \sum_{k=1}^{n} \frac{p_k}{8\Omega_k\Gamma_k} \coth\left[\frac{\beta}{2}\left(\Omega_k + i\Gamma_k\right) e^{i\Omega_k t - \Gamma_k t}\right] + \sum_{k=1}^{n} \frac{p_k}{8\Omega_k\Gamma_k} \coth\left[\frac{\beta}{2}\left(\Omega_k - i\Gamma_k\right) e^{-i\Omega_k t - \Gamma_k t}\right] \\
&\quad + \frac{2i}{\beta} \sum_{k=1}^{n'} J(i\nu_k) e^{-\nu_k t}, \\
b(t) &= \sum_{k=1}^{n} \frac{ip_k}{8\Omega_k\Gamma_k} \left(e^{i\Omega_k t - \Gamma_k t} - e^{-i\Omega_k t - \Gamma_k t}\right),
\end{aligned}
\tag{S9}
$$

with the Matsubara frequencies $\nu_k = 2\pi k/\beta$.

Next, we rewrite the correlation functions as $a(t) = \sum_{k=1}^{n_r} \alpha_k^r e^{\gamma_k^r t}$ and $b(t) = \sum_{k=1}^{n_i} \alpha_k^i e^{\gamma_k^i t}$ with $n_i = 2n$, $n_r = 2n + n'$, where n' is the number of Matsubara frequencies used. Then we define new auxiliary "density matrices" which incorporate both memory effects and initial correlations according to

$$
\begin{aligned}
\rho_k^r(t) &= \lambda \left(\mathcal{T} e^{\int_0^t dt' \mathcal{L}_\mathrm{s}} e^{\gamma_k^r t} \int_0^\infty dt' e^{\mathcal{L}_\mathrm{s} t'} e^{\gamma_k^r t'} \mathcal{L}^- \rho_\mathrm{s}^\mathrm{eq} + \int_0^t dt' e^{\gamma_k^r (t-t')} \mathcal{T} e^{\int_{t'}^t dt'' L_\mathrm{s}} \mathcal{L}^- \rho_\mathrm{s}(t') \right), \\
\rho_k^i(t) &= \lambda \left(\mathcal{T} e^{\int_0^t dt' \mathcal{L}_\mathrm{s}} e^{\gamma_k^i t} \int_0^\infty dt' e^{\mathcal{L}_s t'} e^{\gamma_k^i t'} \mathcal{L}^+ \rho_s^\mathrm{eq} + \int_0^t dt' e^{\gamma_k^i (t-t')} \mathcal{T} e^{\int_{t'}^t dt'' L_\mathrm{s}} \mathcal{L}^+ \rho_\mathrm{s}(t') \right).
\end{aligned}
\tag{S10}
$$

The time-retarded Eq. (S3) (first term) can the be deconvoluted into a set of coupled first-order equations in the form

$$
\begin{aligned}
\dot{\rho}_\mathrm{s}(t) &= \mathcal{L}_\mathrm{s}^\mathrm{eff}(t)\rho_\mathrm{s}(t) + \lambda \left[\sum_{k=1}^{n_r} \alpha_k^r \mathcal{L}^- \rho_k^r(t) + \sum_{k=1}^{n_i} \alpha_k^i \mathcal{L}^- \rho_k^i(t) \right], \\
\dot{\rho}_k^r(t) &= [\mathcal{L}_\mathrm{s}(t) + \gamma_k^r]\rho_k^r(t) + \lambda \mathcal{L}^- \rho_\mathrm{s}(t), k = 1, \ldots, n_r, \\
\dot{\rho}_k^i(t) &= [\mathcal{L}_\mathrm{s}(t) + \gamma_k^i]\rho_k^i(t) + \lambda \mathcal{L}^+ \rho_\mathrm{s}(t), k = 1, \ldots, n_i.
\end{aligned}
\tag{S11}
$$

This set of time non-local quantum master equations was used for the calculations of the quantum system dynamics.

Calculation of the absorption and the circular dichroism (CD) spectrum

We have used the first-order transition dipole moment correlation function to calculate the absorption and the circular dichroism spectra using the expressions

$$
\begin{aligned}
I(\omega) &\propto \omega \int_{-\infty}^{+\infty} dt e^{i\omega t} \langle \boldsymbol{\mu}(t) \boldsymbol{\mu}(0) \rangle_g, \\
CD(\omega) &\propto \omega \int_{-\infty}^{+\infty} dt e^{i\omega t} \langle \boldsymbol{R}_{m,n} \cdot \boldsymbol{\mu}_m \times \boldsymbol{\mu}_n(t) \rangle_g.
\end{aligned}
\tag{S12}
$$

Here, $\boldsymbol{\mu}$ is the transition dipole moment, the subscript g means performing the trace in the correlation function over a thermally equilibrated bath, and, $\boldsymbol{R}_{m,n}$ is the position vector between monomers m and n. The correlation function can be calculated as $\langle \boldsymbol{\mu}(t)\boldsymbol{\mu}(0)\rangle_g = \mathrm{tr_s}\{\boldsymbol{\mu}\mathrm{tr_b}[e^{-iHt}\boldsymbol{\mu}\rho_g e^{iHt}]\}$, $\langle \boldsymbol{R}_{m,n}\cdot\boldsymbol{\mu}_m \times \boldsymbol{\mu}_n(t)\rangle_g = \mathrm{tr_s}\{\boldsymbol{R}_{m,n}\cdot\boldsymbol{\mu}_m \times \mathrm{tr_b}[e^{-iHt}\boldsymbol{\mu}_n\rho_g e^{iHt}]\}$.

Calculation of 2D electronic spectra

For the calculation of the 2D spectra we have applied the equation of motion-phase matching approach (EOM-PMA) proposed by Gelin et al. (*13*). In the EOM-PMA, the induced polarization in the photon-echo direction is calculated by simultaneous propagation of three auxiliary density matrices (ρ_1, ρ_2, ρ_3), each of which obeys a modified equation of motion of the form

$$\begin{aligned}
\dot{\rho_1}(t) &= -i[H_s - V_1(t,t_1) - V_2^\dagger(t,t_2) - V_3^\dagger(t,t_3), \rho_1(t)] - \Re(t)\rho_1(t),\\
\dot{\rho_2}(t) &= -i[H_s - V_1(t,t_1) - V_2^\dagger(t,t_2), \rho_2(t)] - \Re(t)\rho_2(t),\\
\dot{\rho_3}(t) &= -i[H_s - V_1(t,t_1) - V_3^\dagger(t,t_3), \rho_3(t)] - \Re(t)\rho_3(t),
\end{aligned} \tag{S13}$$

where $V_\alpha(t,t_\alpha) = XAe^{-(t-t_\alpha)^2/2\Gamma^2}e^{i\omega t}$, X, Γ are the transition dipole operator and pulse duration, respectively, and $\Re$ is a relaxation superoperator. All three above master equations were calculated by the time non-local quantum master equation Eq. (S11) with the respective different time-dependent Hamiltonians. Then, the third-order induced polarization can be synthesized as

$$P_{PE}(t_1,t_2,t_3,t) = e^{i\mathbf{k_s}\cdot\mathbf{r}}\langle X(\rho_1(t) - \rho_2(t) - \rho_3(t))\rangle + c.c., \tag{S14}$$

where the brackets $\langle \ldots \rangle$ indicate the evaluation of the trace.

The total 2D Fourier-transformed spectrum is then given by the double Fourier transform of the photon-echo polarization signal with respect to τ (which is the time delay between t_1 and t_2) and t, i.e.,

$$S_{PE}(\omega_\tau, T, \omega_t) \sim \int d\tau \int dt\, e^{-i\omega_\tau\tau}e^{i\omega_t t}P_{PE}(\tau,T,t), \tag{S15}$$

where ω_τ is the "coherence" frequency, ω_t is the detection frequency, and T is "waiting" time (delay between t_2 and t_3).

For the calculation of the 2D spectra of the FMO complex, a multi-processing interface has been used to reduce simulation time. The coherent time period $[-300, 300]$ fs has been split up into steps of size $d\tau = 10$ fs and each specified time was sent to one CPU for the calculation. 500 realizations were calculated to account for the random rotation of the molecular transition dipole moment and for static disorder. Therefore, 61 CPUs were used for the calculation of one spectrum. For each CPU, the maximally available memory space of 3.5 GByte was used to speed up the calculation.

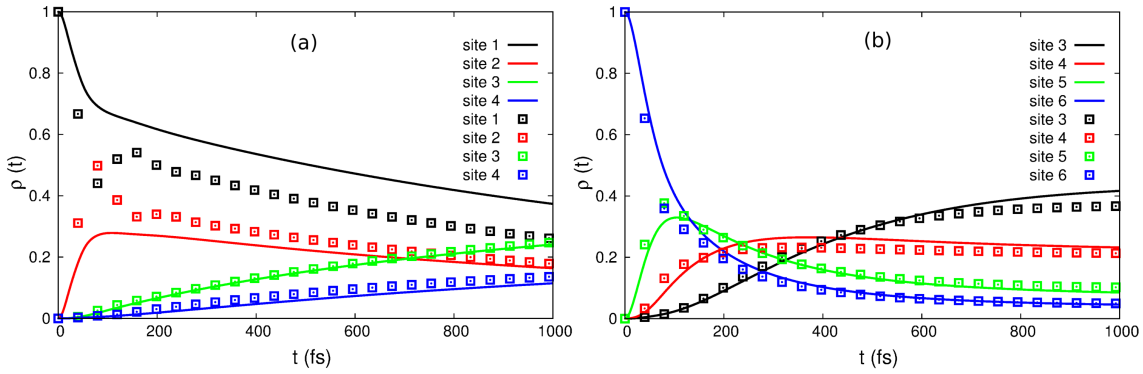

Figure S4: Time-dependent populations of the FMO sites $1-4$ (a) and $3-6$ (b) obtained for the initial preparation in site 1 (a) or in site 6 (b). The solid lines mark the results obtained from a time-nonlocal quantum master equation used in this work together with the spectral density Eq. (S1). The symbols show the results of an exact path-integral calculations (*15*) on the basis of an independently obtained and parametrized experimental spectral density (*14*).

Dynamics of the population of the FMO sites

The spectral density given in Eq. (S1) is the result of a simultaneous fitting to the experimental photon absorption and circular dichroism spectra. A further test of its reliability can be obtained by comparing the resulting dynamics of the FMO site populations obtained with the spectral density of Eq. (S1) and that one obtained previously from numerically exact path integral calculations with an independently obtained and parametrized experimental spectral density (*14*). To be specific, we use the numerically exact results of Ref. 15 as a reference and consider the two cases in which either site 1 or 6 is chosen as the initial state. The system Hamiltonian used in Ref. 15 is exactly the same as used here. The spectral density of Ref. 14 used in Ref. 15 is different from that of Eq. (S1). The low-frequency part of Eq. (S1) is Ohmic while that one of Ref. 14 is super-Ohmic. The high-frequency parts are also different, but we note that the interesting long-time dynamics is governed by the low-frequency parts of the bath spectral density. The comparison is shown in Fig. S4 for a temperature of 300 K. We find a good agreement especially at long times while the deviations at short times are due to the differences in the high-frequency sections of the two different spectral densities.

Low-temperature calculations

In order to check the performance of the modeling and the reliability of the approach in terms of a quantum dissipative dynamics, we consider in this section the impact of changing the temperature, but keeping all other parameters unchanged. For this, we have calculated the linear absorption and CD spectra at 77 K. The calculated results are shown in Fig. S5 (red solid lines) together with the experimentally measured data taken from Ref. 16. We find a good agreement

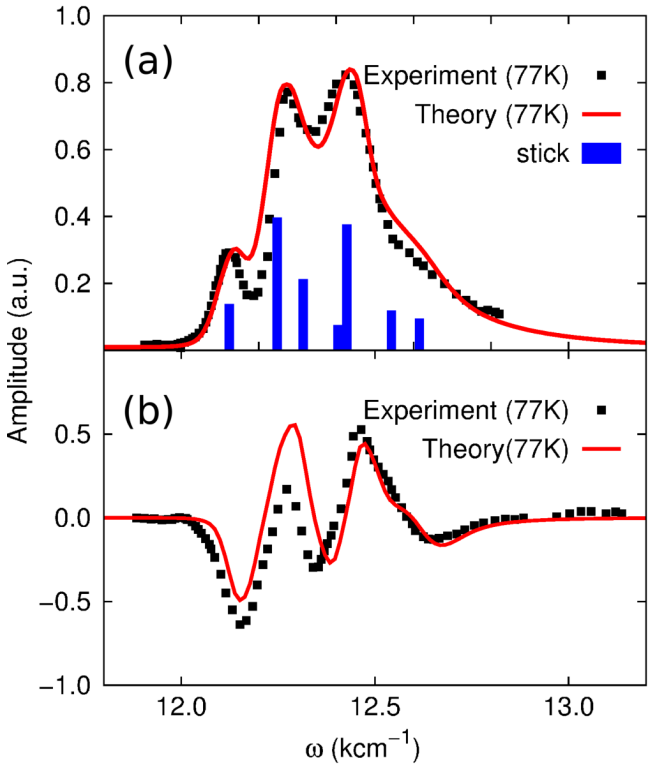

Figure S5: (a) Linear absorption spectrum and (b) circular dichroism spectrum of the FMO complex at 77 K. The solid red lines show the theoretical results obtained with the same parameter set used throughout this work, but with the only modified parameter being temperature. The square symbols mark the experimental results taken from Ref. 16. The blue bars in (a) mark the stick spectrum of the FMO complex.

given the fact that we the only changing parameter is temperature.

In addition, we have calculated the 2D electronic spectra of the FMO complex at 77 K as well with the same set of parameters. The results for different waiting times are shown in Fig. S6. The spectra are in good agreement with the experimental results (*17, 18*). The energy transfer dynamics and pathways can be clearly observed by the kinetics of the off-diagonal peaks.

Moreover, we calculate the time evolution of the off-diagonal signal at the spectral position ($\omega_\tau = 12350$ cm^{-1}, $\omega_t = 12200$ cm^{-1}) considered in Ref. 19 and marked by "X" in Fig. 1A in the main paper, but now also for 77 K. Apart from changing temperature, we use the same parameters as before and the spectral density of Eq. (S1). The results for the real and imaginary parts are shown in Fig. S7. We find only weak electronic coherence which vanishes within the dephasing time of less than 200 fs. As a consistence check, we also measure the homogeneous linewidth provided by the antidiagonal in Fig. S6 for zero waiting time. We find a FWHM of

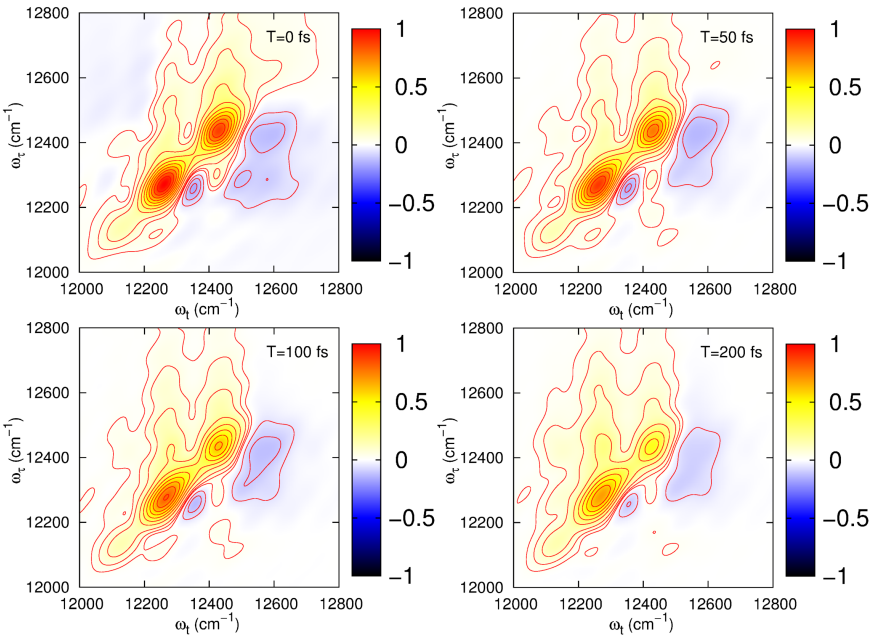

Figure S6: Real part of the 2D photon echo spectra calculated for a temperature of 77 K for selected waiting times as indicated. Notice that the two axes for ω_τ and ω_t are swapped as compared to Ref. (*17*).

$\Delta_{\mathrm{hom}} = 90\ \mathrm{cm}^{-1}$. This corresponds to an electronic dephasing time of $\tau_{\mathrm{hom}} = 120$ fs at 77 K, in agreement with the previous results. Hence, we cannot confirm long-lived electronic coherence at a temperature of 77K reported up to times beyond 1 ps.

Simulating long-lived electronic coherence

We did not observe long-lived electronic coherence in the present experimental and theoretical results of the FMO complex. However, we can consider the question how a long-lived electronic coherence would show up in an optical 2D spectrum at low temperature and, consistently, in the time-dependent off-diagonal signal. To answer this question, we have used the simplest possible model of a pure Ohmic spectral density, i.e., only the first term of Eq. (S1) and mimic long-lived electronic coherence by a very weak system-bath interaction. We set $\gamma = 0.35$ and $\omega_c = 100\ \mathrm{cm}^{-1}$, and set the temperature again to 77 K. In Fig. S8 (a), we show the result of the 2D spectrum of the FMO under these weak-coupling conditions. The weak system-bath coupling induces a very narrow central peak with a small homogeneous broadening visible in the antidiagonal band width. We extract a FWHM of $\Delta_{\mathrm{hom}} = 25\ \mathrm{cm}^{-1}$. This corresponds to an electronic dephasing time of $\tau_{\mathrm{hom}} = 420$ fs.

Correspondingly, we show in Fig. S8 (b) the time-dependent off-diagonal signal at the spec-

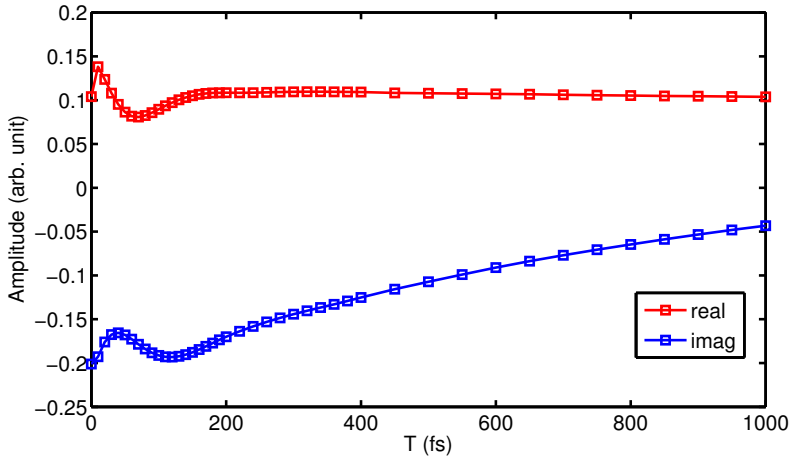

Figure S7: Calculated time-dependent off-diagonal signal (red: real part, blue: imaginary part) at the spectral position ($\omega_\tau = 12350$ cm^{-1}, $\omega_t = 12200$ cm^{-1}) considered in Ref. 19 and marked by "X" in Fig. 1A in the main paper, but now for 77 K.

tral position ($\omega_\tau = 12350$ cm^{-1}, $\omega_t = 12200$ cm^{-1}) considered in Ref. 19 and marked by "X" in Fig. 1A in the main paper. We find (artificially created) long-lived electronic coherence up to times beyond 450 fs, in agreement with the findings from the homogeneous line width. However, the measured 2D spectra of the real FMO complex do not show these sharp ridges with a very narrow diagonal peaks at zero waiting times.

Three-dimensional spectrum of residuals in 2D data

After obtaining the residuals by removing the kinetics from the experimental data, we have applied a numerical Fourier transform to the real part with equally separated time steps (10 fs) up to 2 ps. This yields a three-dimensional spectrum of the residuals with the dimensions ω_t, ω_τ and the vibrational frequency in the waiting time domain, ω_T. A few representative two-dimensional vibrational maps with relatively large magnitudes and obtained from the experimental data are shown for different vibrational frequencies ω_T in Figs. S9 and S10. In order to prove the reproducibility of the observed vibrational oscillations, we present four data sets labeled by (1), (2), (3) and (4) of repeated measurements. In sets (1) and (2), the data were taken with a low power excitation pulse (with ~ 8 nJ), while in sets (3) and (4), we have chosen excitation pulse with ~ 12 nJ. It shows that the presented vibrational oscillations and the underlying frequencies are fully reproducible in four independent measurements although the excitation power was different.

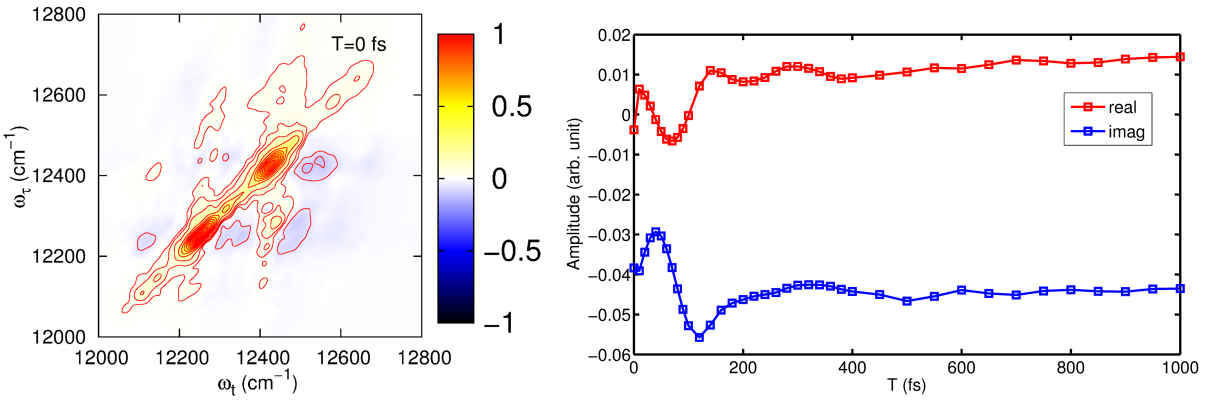

Figure S8: (a) Calculated 2D spectrum of the FMO under artificially assumed weak system-bath conditions with an Ohmic spectral density with $\gamma = 0.35$ and $\omega_c = 100$ cm^{-1}, and temperature of 77 K. Notice that the two axes for ω_τ and ω_t are swapped as compared to Ref. (*17*). (b) Extracted time-dependent off-diagonal signal at the spectral position ($\omega_\tau = 12350$ cm^{-1}, $\omega_t = 12200$ cm^{-1}) considered in Ref. 19 and marked by "X" in Fig. 1A in the main paper.

Correlation analysis of the 2D vibrational maps

In order to quantify the correlation in the presented 2D vibrational maps, we perform a 2D correlation analysis of the different sets of measurements which are labeled as (1) to (4) in Fig. S9 and S10. The correlation parameters are shown in Table 1.

Items	596	628	725	741	838	1015	1112	1144	1289	1595
1↔2	0.9218	0.8892	0.8571	0.7863	0.7531	0.7808	0.5801	0.8878	0.9202	0.7287
1↔3	0.6289	0.7929	0.7568	0.8485	0.6650	0.8688	0.5220	0.7912	0.7773	0.7065
1↔4	0.6591	0.7278	0.5807	0.6281	0.6190	0.8742	0.5826	0.7748	0.4268	0.6262
2↔3	0.7945	0.6009	0.7844	0.9047	0.4902	0.6668	0.8353	0.7655	0.8232	0.8208
2↔4	0.7600	0.5453	0.5885	0.6458	0.5040	0.6523	0.7551	0.7516	0.4439	0.7965
3↔4	0.8686	0.9498	0.7682	0.7624	0.9178	0.9514	0.4668	0.9739	0.6836	0.9409

Table 1: The 2D correlation analysis of the 2D vibrational maps. The vibrational frequencies are given in units of cm^{-1}.

Time-dependent off-diagonal signal at the X position

In Fig. 3C of the main paper, we show the time-dependent off-diagonal signal at the spectral position ($\omega_\tau = 12350$, $\omega_t = 12200$cm-1) considered in Ref. 19 and marked by "X" in Fig. 1A in the main paper for waiting times up to 600 fs. In Fig. S11, we provide the results for the time window between 600 fs and 2 ps in order to illustrate that no long-time electronic coherence is present up to this time. The data are the averages of four independently measured spectra with

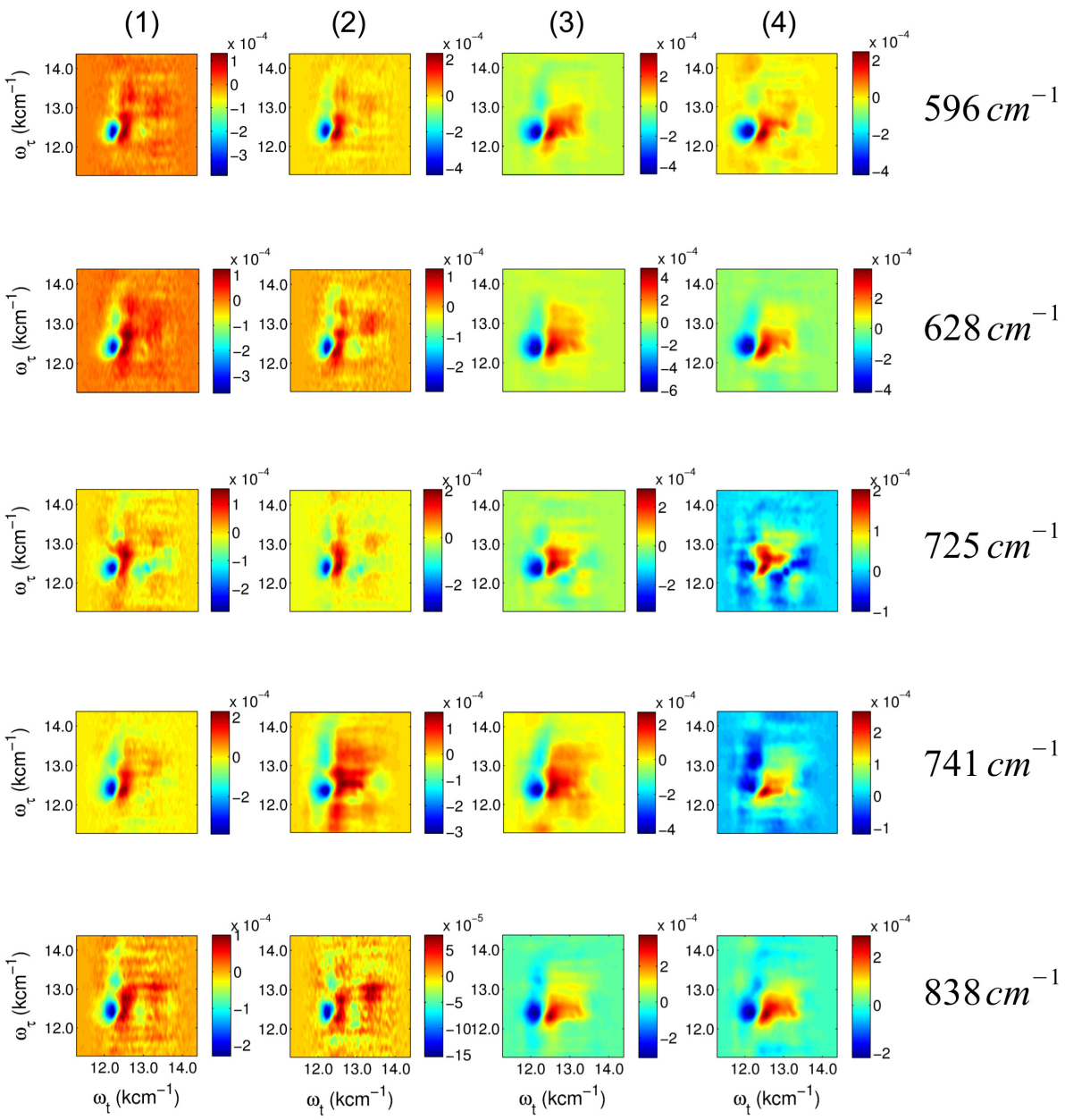

Figure S9: Two-dimensional vibrational map (ω_t, ω_τ) for different values of the frequency ω_T from 596 cm^{-1} to 838 cm^{-1}. Shown are four independent measurements with different values of the pulse excitation power. In sets (1) and (2), we have chosen $\sim$ 8 nJ and in sets (3) and (4), the excitation power was set to $\sim$ 12 nJ. All show good agreement and reproducibility.

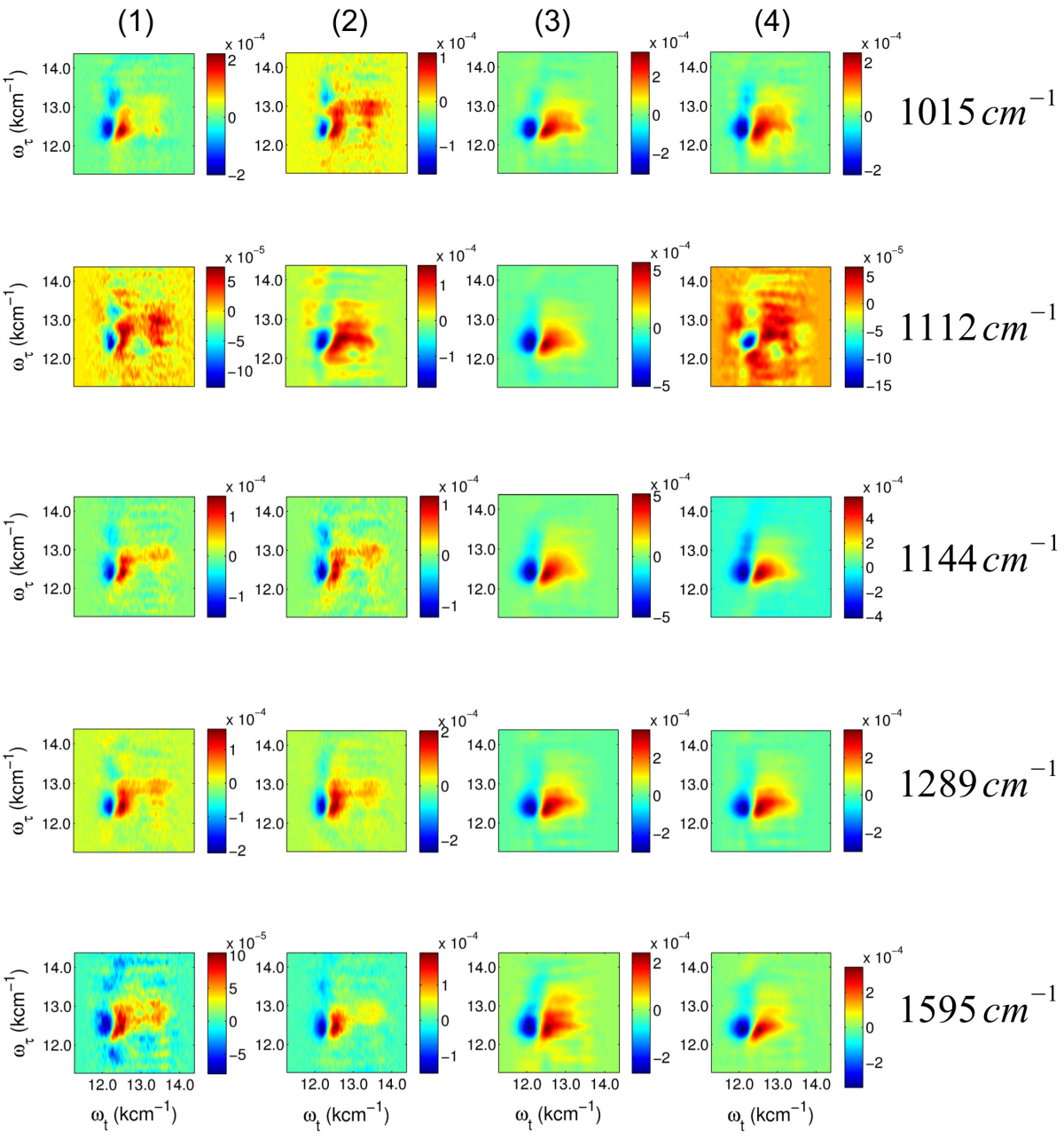

Figure S10: Same as in Fig. S9, but for the frequencies ω_T from 1015 cm^{-1} to 1595 cm^{-1}.

the resulting standard deviation shown as error bars.

Finally, we have calculated the Fourier spectrum of this average, which is shown in Fig.

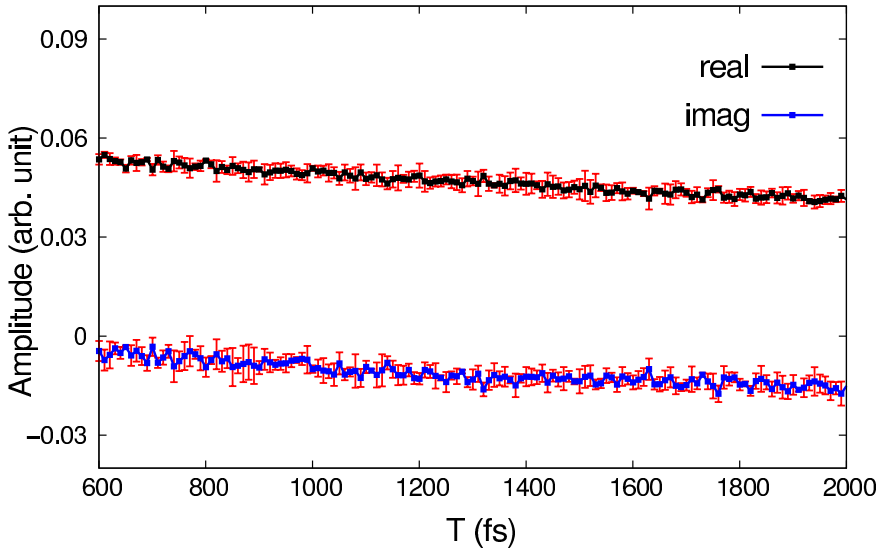

Figure S11: Time-dependent off-diagonal signal at the spectral position ($\omega_\tau = 12350$, $\omega_t = 12200$cm-1) considered in Ref. 19 and marked by "X" in Fig. 1A in the main paper for waiting times between 600 fs and 2 ps. The error bars mark the standard deviation obtained after averaging four available experimental spectra.

S12. We do not find any pronounced frequency component.

Relation between the anti-diagonal bandwidth and the homogeneous line width

In order to demonstrate that the exciton dynamics in the FMO complex operates in the fast modulation limit, we have investigated the time dependence of the frequency correlation function $M(T)$ (*20, 21*). For a given waiting time T, it can be extracted from the 2D electronic spectra in the form of the ellipse eccentricity of the central peak according to the ratio

$$M(T) = \frac{(a^2 - b^2)}{(a^2 + b^2)}\,, \tag{S16}$$

where a is the major and b the minor axis of the ellipse, see Fig. S13. When this function decays exponentially with increasing T, the dynamics occurs in the fast modulation (or homogeneous) limit. Put differently, the time scales of the homogeneous and inhomogeneous broadening are well separated and an effective Markovian dynamics occurs. Then, the antidiagonal band width coincides with the electronic dephasing time (*20, 21*). Here, we have measured the time-evolved diagonal (a) and anti-diagonal (b) bandwidth from the 2D spectra for different waiting times T. The frequency correlation function $M(T)$ is plotted in Fig. S13 and shows a clear exponential decay at short to intermediate times (< 500 fs). Due to the admixture from the vibrational progression and the energy transfer (excited state absorption), it deviates from a

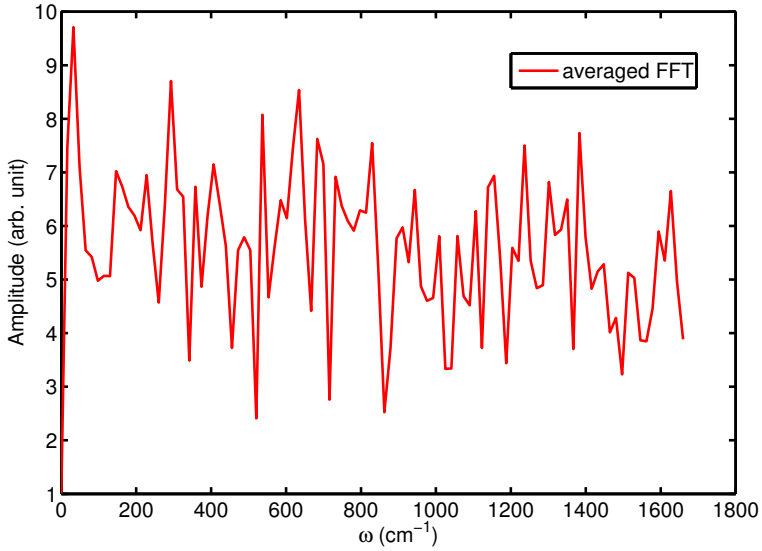

Figure S12: Fourier spectrum of the full time trace shown in Fig. 3C in the main paper and in Fig. S11.

clean single-exponential function at asymptotic times. Hence, we can safely conclude that we are in the Markovian (fast modulation) regime which confirms earlier findings (*22*) on the basis of numerically exact path-integral calculations of the non-Markovianity measure of the exciton dynamics of the FMO complex.

References

1. Azai C, Kim K, Kondo T, Harada J, Itoh S, Oh-Oka H (2011) A heterogeneous tag-attachment to the homodimeric type 1 photosynthetic reaction center core protein in the green sulfur bacterium Chlorobaculum tepidum. *Biochim Biophys Acta* 1807:803-812.

2. Wahlund TM, Woese CR, Castenholz RW, Madigan MT (1991) A thermophilic green sulfur bacterium from New Zealand hot springs, Chlorobium tepidum sp. nov. *Arch Microbiol* 156:81-90.

3. Oh-Oka H, Kamei S, Matsubara H, Iwaki M, Itoh S (1995) Two molecules of cytochrome c function as the electron donors to P840 in the reaction center complex isolated from a green sulfur bacterium, Chlorobium tepidum. *FEBS Lett* 365: 30-34.

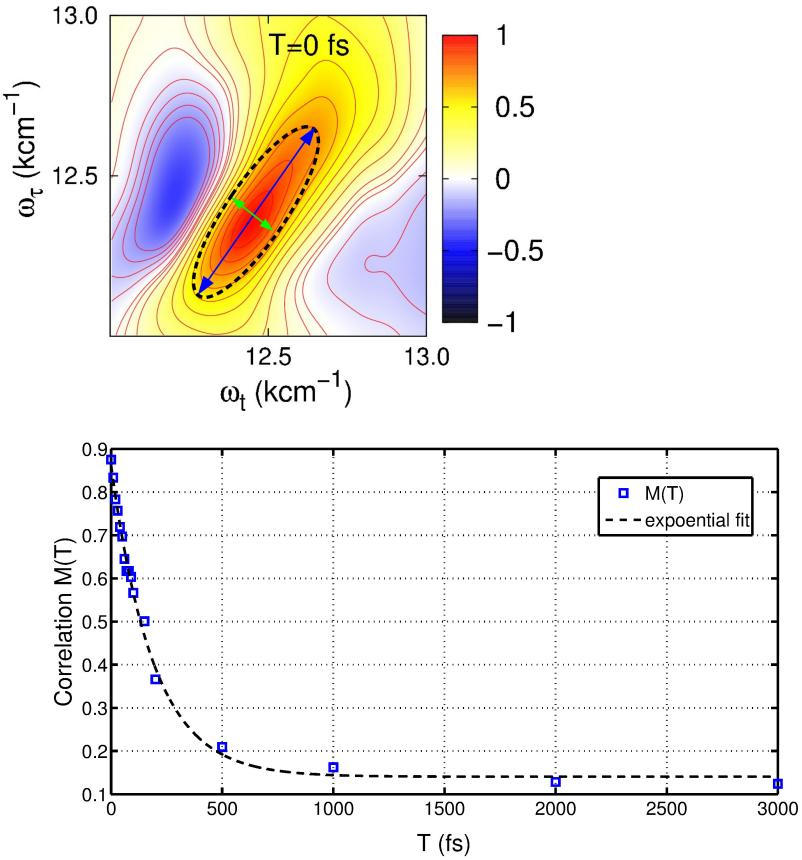

Figure S13: Time-evolution of the correlation function $M(T)$ calculated from the diagonal and anti-diagonal bandwidth. The dynamics can be well fitted by one exponential function, which clearly manifests the Markovian dynamics.

4. Kelly SM, Jess TJ, Price NC (2005) How to study proteins by circular dichroism. *Biochim Biophys Acta* 1751:119-139.

5. Greenfield NJ (2007) Using circular dichroism spectra to estimate protein secondary structure. *Nat Protoc* 1:2876-2890.

6. Gelzinis A, Valkunas L, Fuller FD, Ogilvie JP, Mukamel S, Abramavicius D (2013) Tight-binding model of the photosystem II reaction center: application to two-dimensional electronic spectroscopy. *New J Phys* 15:075013.

7. Meier C, Tannor DJ (1999) Non-Markovian evolution of the density operator in the pres-

ence of strong laser fields. *J Chem Phys* 111: 3365-3376.

8. Kleinekathöfer U (2004) Non-Markovian theories based on a decomposition of the spectral density. *J Chem Phys* 121:2505-2514.

9. Zwanzig R (1961) Statistical mechanics of irreversibility. *Lectures in Theoretical Physics (Boulder) Vol 3*, eds Britten WE, Downs BW, Downs J (Interscience, New York), pp 106 - 141.

10. Morillo M, Cukier RI (1997) Controlling low-temperature tunneling dynamics with external fields. *Phys Rev B* 54:13962-13973.

11. Kleinekathöfer U, Barvík I, Heřman P, Kondov I, Schreiber M (2003) Memory effects in the fluorescence depolarization dynamics studied within the B850 ring of purple bacteria. *J Phys Chem B* 107:14094-14102.

12. Ritschel G, Eisfeld A (2014) Analytic representations of bath correlation functions for ohmic and superohmic spectral densities using simple poles. *J Chem Phys* 141:094101.

13. Gelin MF, Egorova D, Domcke W (2005) Efficient method for the calculation of time- and frequency-resolved four-wave mixing signals and its application to photon-echo spectroscopy. *J Chem Phys* 123:164112.

14. Adolphs J, Renger T (2006) How Proteins Trigger Excitation Energy Transfer in the FMO Complex of Green Sulfur Bacteria. *Biophys J* 91:2778-2797.

15. Nalbach P, Braun D, Thorwart M (2011) Exciton transfer dynamics and quantumness of energy transfer in the Fenna-Matthews-Olson complex. *Phys Rev E* 84:041926.

16. Melkozernov AN, Olson JM, Li YF, Allen JP, Blankenship RE (1998) Orientation and excitonic interactions in the Fenna-Matthews-Olson bacteriochlorophyll a protein in membranes of the green sulfur bacterium Chlorobium tepidum. *Photosynth Res* 56: 315-328.

17. Thyrhaug E, Židek K, Dostál J, Bina D, Zigmantas D (2016) Exciton structure and energy transfer in the Fenna-Matthews-Olson complex. *J Phys Chem Lett* 7:1653-1660.

18. Brixner T, Stenger J, Vaswani HM, Cho M, Blankenship RE, Fleming GR (2005) Two-dimensional spectroscopy of electronic couplings in photosynthesis. *Nature* 434:625-628.

19. Panitchayangkoon G et al. (2010) Long-lived quantum coherence in photosynthetic complexes at physiological temperature. *Proc Natl Acad Sci USA* 107:12766-12770.

20. Hamm P, Zanni M (2011) Homogeneous and inhomogeneous dynamics. *Concepts and Methods of 2D Infrared Spectroscopy* (Cambridge University Press, Cambridge), pp 152 - 164.

21. Lazonder K, Pshenichnikov MS, Wiersma DA (2007) Two-dimensional optical correlation spectroscopy applied to liquid/glass dynamics. *Ultrafast Phenomena XV, Proceedings of the 15th International Conference*, eds Corkum P, Jonas DM, Miller RJD, Weiner AM (Springer, Berlin), pp 356 - 358.

22. Mujica-Martinez C, Nalbach P, Thorwart M (2013) Quantification of non-Markovian effects in the Fenna-Matthews-Olson complex. *Phys Rev E* 88:062719.